Received: June 1, 2023. Revised: July 8, 2023.

INASS

International Journal of
Intelligent Engineering & Systems

http://www.inass.org/

Design of Barnacle Mating Optimizer with Deep Learning Based Classification Model for Medical X-Ray Images

T. Kumar[1]* R. Ponnusamy[1]

[1]*Department of Computer and Information Science, Annamalai University, Annamalai Nagar, India*
* Corresponding auther's Email: kumarddeau@gmail.com

Abstract: Classification of medical X-Ray image (XRI) is a task where machine learning (ML) approaches are utilized to categorize XRIs into various categories on the basis of some criteria. The core objective is to automate the task of evaluating XRIs and enhance the efficiency and accuracy of diagnosis. Current advancements in deep learning (DL) have given rise to better performance in various medical image analysis processes. Chest radiographs, the frequently performed radiological exam, are specifically significant modalities for which various applications were studied. The issue of publicly available, multiple, large chest X-Ray datasets in recent times has increased investigation. Therefore, this article presents a new barnacles mating optimizer with DL based medical image classification model (BMODL-MICM) for XRIs. The BMODL-MICM technique uses wiener filtering (WF) as a preprocessing step to eradicate the noise. Besides, the ShuffleNetv2 feature extractor is involved to create a collection of feature vectors. Moreover, the BMODL-MICM technique uses the BMO algorithm for the hyperparameter tuning procedure. At last, elman neural network (ENN) technique is applied for XRIs classification. The investigational assessment of the BMODL-MICM approach on the benchmark XRI dataset reported its effectual outcome of 99.67% over the other methods.

Keywords: Medical image classification, X-Ray images, Barnacle's mating optimizer, Deep learning, Chest radiographs.

1. Introduction

Medical imaging has become an effective means for diagnosing diseases in patients like tuberculosis, pneumonia, etc. [1]. A backbone of radiological imaging for several years, chest X-Ray is the frequently achieved radiological examination, with technologically advanced nations reporting nearly 238 erect viewing CXR imaging obtained per 1000 populace every year [2]. The availability and demand for CXR images can be recognized as low radiation dose, cost-effectiveness, and reasonable sensitivity to various pathologies [3]. The first imaging study is CXR, which remained dominant in the diagnosis, management, and screening of far reaching of conditions. The analysis of the chest radiograph seems to be a challenge because of the superimposition of anatomical designs and estimate direction [4]. This makes it extremely challenging to identify abnormalities in specific places, spot subtle or minor abnormalities, or precisely differentiate various pathological patterns [5].

ML is broadly utilized in the healthcare domain, and ML methods are used to help doctors to do tasks with a higher level of precision and speed [6]. The subset of ML, DL, is a mathematically devised network to be trained to categorize some input into specified categories [7]. With technological advancements, DL methods are applied to cure diseases, namely pneumonia, arrhythmia, breast cancer, skin cancer, etc [8]. DL methods were used on fundus and CXR images to identify diseases. With advanced technology, hospitals and radiologists can utilize DL methods even working remotely [9]. Currently, DL has proven to be the preferred method for the task of image analysis and had a remarkable effect in the medical imaging domain [10]. DL is particularly data-hungry, and CXR study groups can be helped in the publication of several large labelled datasets in recent times.

This article presents a new barnacles mating optimizer with DL based medical image classification model (BMODL-MICM) for XRIs. The presented BMODL-MICM technique uses wiener filtering (WF) as a preprocessing step to eradicate the noise. Besides, the ShuffleNetv2 feature extractor is involved in creating a feature vector collection. Moreover, the BMODL-MICM technique uses the BMO algorithm for the hyperparameter tuning procedure. At last, elman neural network (ENN) approach is applied for classifying XRIs. The investigational assessment of the BMODL-MICM approach on the benchmark XRI dataset reported its effectual performance over the other compared methods in terms of diverse measures. However, to avert overfitting, certain DL networking should be fine-tuned using metaheuristics like puzzle optimization algorithm (POA) [6], guided pelican algorithm (GPO) [7], stochastic komodo algorithm (SKA) [8], quad tournament optimizer (QTO) [9], multiple interaction optimizer (MIO) [10], etc.

The remaining sections of the article is arranged as. Section 2 offers the related works and section 3 represents the proposed model. Then, section 4 elaborates the results evaluation and section 5 completes the work.

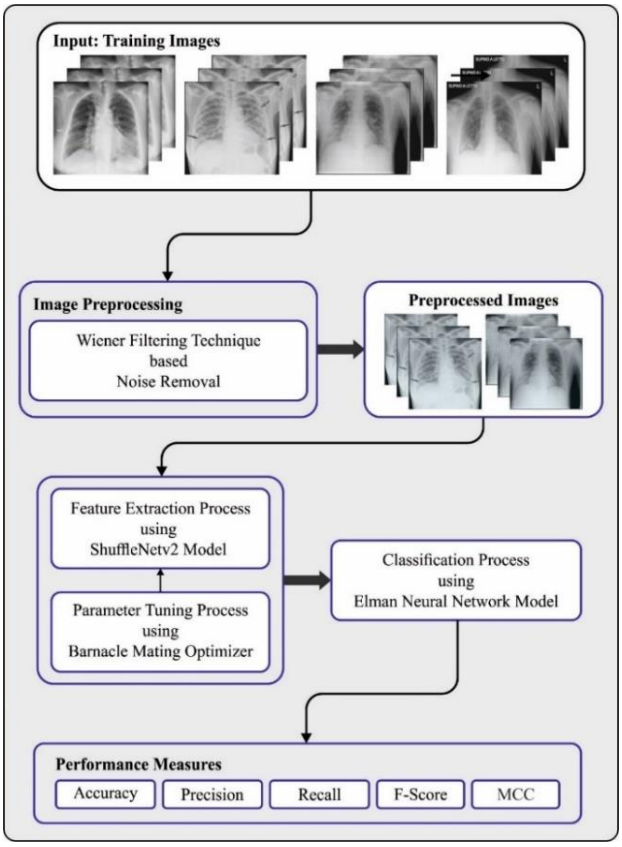

Figure. 1 Work flow of BMODL-MICM approach

2. Related works

Verma et al. [11] present a wavelet and AI enabled efficient and rapid investigation process for patients with SARS-nCoV, i.e., Severe Acute Respiratory Coronavirus Syndrome, using a DL technique from thoracic XRI. To find SARS-nCoV, this study has used a wavelet-based CNN approach. With these thoracic XRIs, CNN is trained end-to-end and pre-trained on ImageNet. In [12], the authors introduce a competitive analysis of knowledge distillation (KD) in DL to classify abnormality in CXR imagery. This technique distils knowledge in burdensome teacher methods into lightweight student or self-training student techniques.

Tanzi et al. [13] targeted to devise a DL related tool that assists physicians in detecting bone fractures. Two methods have been applied: a multistage structure comprising successive CNNs, well-matched to the ranking framework of the OTA or AO classification, and a fine-tuned InceptionV3 CNN employed as a reference for this devised technique. In [14], the authors present an innovative hybrid DL structure by merging VGG, spatial transformer network (STN), and data augmentation, including CNN, which is devised. This technique was adopted for the NIH-CXR image dataset gained from the Kaggle repository.

Chen et al. [15] used XRI recognition devices determination bone age to gain a better identification effect by comparing existing methods. The presented has two steps: the classification method and feature extraction. The feature extraction uses depth NN to learn the LBP and XRI features. The classification technique depends on SVM was applied for feature classification. In [16], a CAD system using CXR images for automated pneumonia recognition is introduced. Here a weighted average ensemble approach has been implemented, where weights allocated to the base learners are ascertained with the help of devised technique. Uysal et al. [17] intend to aid doctors by categorizing shoulder imageries in X-Ray equipment as non- or fracture with AI.

3. The proposed model

In this research, an automated XRI classification model named BMODL-MICM model is presented. The suggested BMODL-MICM model investigates the XRIs thoroughly and allocates proper class labels to them. To accomplish this, the BMODL-MICM approach combines WF, ShuffleNetv2, BMO, and ENN based noise removing, feature extracting, tuning, and classification. Fig. 1 exhibits the work-flow of the BMODL-MICM technique.

3.1 WF based preprocessing

To eliminate the noise in the XRIs, the BMODL-MICM approach uses the WF technique. To predict the original signal, a statistical algorithm uses a mathematical approach to the image and the noise [18]. The WF functions by analyzing the power spectrum of noise and the signal. The power spectrum can be defined as a measure of the volume of energy in the noise and signal at various frequencies. The WF utilizes this data to eradicate the noises from the signal and preserve the significant features of the imagery. The fundamental steps indulged in WF based noise removal are:

Acquire the degraded images: The initial step is to acquire the images that were degraded by noise.

Predict the power spectrum of the signal and the noise: The next step is to predict the power spectrum of the noise and the signal. This can be performed through statistical techniques like autocorrelation.

Calculate the WF: The WF is computed through the estimated power spectra of noise and the signal. The WF denotes a frequency domain filter utilized for eradicating noise from the degraded images.

Apply the WF: The last phase is to apply the WF to the degraded image. This will eradicate the noises in the images and restore the original signal.

3.2 ShuffleNetv2 feature extractor

For the derivation of the feature vectors, the ShuffleNet model is used. Due to the advancement of DL technology, the concept of CNN has quickly expanded in the past few years [19]. Considering an FCN with different layers that will be simulating the human being's brain structure, a CNN could implement recognition and supervised learning directly from images. CNN is primarily comprised of FC, input, convolutional, ReLU, and Pooling layers. By collectively stacking those layers, a complete CNN is created. CNN is greater at video processing, which is a super-positioning of imaging. Typically, it can be utilized in security medicine, automated driving, etc.

But with NN becoming deep and more profound, computation difficulty rises considerably, which stimulated the appearance of the lightweight structure involving Xception, MobileNetV2, ShuffleNetVl, and ShuffleNetV2. The ShuffleNetV2 has the highest speed and accuracy among the four different structures. Thus, ShuffleNetV2 is used as the front end of the model. It primarily exploits two new operations, such as channel shuffle and pointwise GC, that decrease the computation cost without affecting detection performance.

Group convolution (GC) was initially applied in AlexNet to distribute the network through 2 GPUs, which proves its efficiency in ResNeXt. The conventional convolution (CC) implements a channel-dense connection that implements a convolutional function on all the channels of the input feature.

For the CC, the height and width of the kernels are K, and the C characterizes the amount of input channels; when the count of the output channel is N, then the count of kernels is N. The parameter count can be evaluated as follows:

$$P(CC) = K \times K \times C \times N\ (parameters) \quad (1)$$

For GC, the channel of the input feature was split into G groups, so the count of kernels is C/G; the outcomes from G groups were concatenated as large feature output of $the\ N$ channel. The parameter count can be evaluated as follows:

$$P(GC) = K \times K \times \frac{C}{G} \times N\ (parameters) \quad (2)$$

From the equation, the parameter count in GC is smaller than in CC. But GC results in the issue that multiple groups will not be able to share data. In the ShuffleNetV2 unit, a channel split was initially implemented on the input feature maps that can be equally split in to two branches. The left branch remained the same, while the right branch experiences three convolutional functions. Once the convolutional is finished, the two branches are joined to fuse the feature. Lastly, channel shuffle has been utilized for communicating data among various groups.

In the ShuffleNetV2 unit, the channels are not split, and the feature map can be inputted directly toward the two branches. These two branches exploit 3x3 deep complex layers to decrease the dimension of the maps. Next, the concatenation function was implemented on the output of two branches.

3.3 Hyperparameter tuning using BMO algorithm

In this work, the BMO model adjusts the hyperparameter values of the ShuffleNetv2 method. This model is stimulated by the nature of barnacles, and it combines diverse phases as defined below [20]. The section offers the scientific expression of BMO.

Stage 1: Initialization

Primarily, the candidate solution is denoted as follows. This phase includes the generation of candidate outcomes that are created arbitrarily. The

assessment can be implemented to attain the primary candidate solutions in the next sorting stage:

$$X = \begin{bmatrix} x_l^1 & \cdots & x_1^N \\ \cdots & \cdots & \cdots \\ x_n^l & \cdots & x_n^N \end{bmatrix} \quad (3)$$

In Eq. (3), N shows the dimension of control parameters that has to be improved, while n characterizes the barnacle populace regarded as the candidate. The control variable in (3) is subjected to the boundary of the issue, as shown below:

$$ub = [ub_1, \ldots, ub_i] \quad (4)$$

$$lb = [lb_1, \ldots, lb_j] \quad (5)$$

Lb and ub is the lower and upper bound of ith parameters.

Stage 2: Selection

The selecting task for mating to create novel progenies was done arbitrarily. But it is subjected to a variable that should be hyper tuned called pl that signifies the barnacle's range that could be able to mate. Barnacles were categorized as hermaphroditic organisms that contributes to and obtains sperm from other members. Consider that a single barnacle can fertilize every barnacle.

Phase 3: Reproduction

According to the Hardy-Weinberg rule, the reproduction of novel offspring constituted the features in the parents were inherited as:

$$x_i^{N_{new}} = px_{barnacles}^N + qx_{banacle_m}^N \quad (6)$$

In Eq. (6), p specifies the normal dispersion of random numbers within [0,1], $q = 1 - p$, $x_{barnacles\_d}^N$ and $x_{barnacle\_m}^N$ signify the parameter of dad and mum (D&M) barnacles, respectively. Consider that p and q signify the amount of features handed-down from D&M, respectively, to generate next progenies. The offspring inherit the feature from parents based on the arbitrary values' probability within [0, 1]. For instance, if p (generated randomly), it implies that the new offspring is 45% of the factors of Mum and inherits 55% of the feature of Dad. Also, (6) is the exploitation procedure of the BMO to obtain novel solutions. The exploration and exploitation procedures in BMO rely greatly on pl. Exploitation takes place, and (6) is applied when the barnacle's selection that went through mating falls under the barnacle's range chosen from the D&M. Sperm cast takes place once the barnacle selection that should be mated surpasses the pl value, and it can be shown as:

$$x_i^{nnew} = rand(\,) \times x_{barnacleM}^N \quad (7)$$

Algorithm 1: Pseudocode of BMBO

Population initialization of barnacle:

$X_i = rand(n, 2)$

Compute the Fitness Function (FF) of all the barnacles

$Fitness = calculate\_fitness(X_i)$

Sort to locate the better results at the top of the population (T=the better solution):

$[sorted_{fitness}, idx] = sort(fitness(X_i)$

$T = X_i(idx(1), :)$

$While(I < Maximum\ iterations)$:

$for\ I = l: Max\_iter$

Set the value of $the\ p^l$

Selection based on the equation as follows:

$barnacle\_m = randperm(n)$

$barnacle\_m = randperm(n)$

If the selection of D&M=p^l

$If\ rand() <= p^l$

$for\ i = l: size(X_i, 2)$

Offspring generation based on (4)

$P = rand()$

$q = 1 - p$

$X_i^{N_{new}} = px_{barnacles_d}^N z + qx_{barnacle_m}^N$

$end\ for$

$else\ if\ selection\ Dad\ and\ Mum > p^l$

For all the variables

$for\ i = l: size(X_i, 2)$

Offspring generation based on Eq. (7)

$x_i^{n\_new} = rand() \times x_{barnacle\_m}^N$

end for

end if

Bring the present barnacle back if it is out of the boundaries

$for\ i = l: size(X_i\_new, l)$

$for\ j = l: size(X_i\_new, 2)$

$if\ X_i\_new(i, j) < 0$

$X_i\_new(i, j) = 0$

$else\ if\ X_i\_new(i, j) > 1$

$X_i\_new(i, j) = 1$

$end\ if$

$end\ for$

Compute the FF of all the barnacles

$Fitness\_new = calculate\_fitness(X_i\_new)$

Sort and upgrade T if there is a best solution

$if\ sorted\_fitness\_new(l) < sorted\_fitness(l)$

$T = X_i\_new(idx\_new(l), :))$

end

$Update\ X_i\ and\ fitness$
$X_i = X_i\_new$
$Fitness = fitness\_new$
end
end
$I = I + 1$
$end\ while$
Return T

In Eq. (7), $rand()$ signifies the random number within [0, 1].

FF selection becomes a vigorous component of the BMO approach. An encoder solution was adopted for evaluating the goodness of candidate results. The value of accuracy was the major form enforced to devise a FF.

$$Fitness = \max(P) \tag{8}$$

$$P = \frac{TP}{TP+FP} \tag{9}$$

Whereas TP and FP defines the true and false positive value.

3.4 Image classification using ENN model

Finally, the ENN technique was applied for the effectual XRIs classification. ENN technique is classified into four layers: output, input, undertake, and Hidden Layers (HL) [21]. Undertake layer can be applied to remember the HL output that can be observed as step delay operators. Depending on the BP networking, the outputs of HL relate with the input via the storage and delay of undertaken layer. This relation way was sensible to historic datasets, and an interior feedback networking may raise the capability of managing dynamic data.

Suppose with the count of hidden and undertaken neurons are r, n input, m output, the weight of the input and undertaken layer to HL is w_1 and w_2, and of the output layer is w_3; $u(k-1)$ denotes the NNs input, $x(k)$ represents the HL output, $x_c(k)$ indicated the undertake layer output, $y(k)$ signifies the NN output, next.

$$x(k) = f\left(w_2 x_c(k) + w_1\big(u(k-1)\big)\right), \tag{10}$$

Here $x_c(k) = x(k-1)$. f is the HL transfer function that is frequently utilized in S-type function,

$$f(x) = (1 + e^{-x})^{-1} \tag{11}$$

g denotes the output layers transfer function that can always be a linear function, that is, input layer HL output layer

$$y(k) = g\big(w_3 x(k)\big) \tag{12}$$

ENN uses the BP approach for revising weights; the network error is

$$E = \sum_{k=1}^{m}(t_k - y_k)^2, \tag{13}$$

Then t_k denotes the object's output vector.

Table 1. Details of the dataset

Class	Number of Images
COVID-19	1000
Standard	1000
Viral Pneumonia (VP)	1000
Overall Images	**3000**

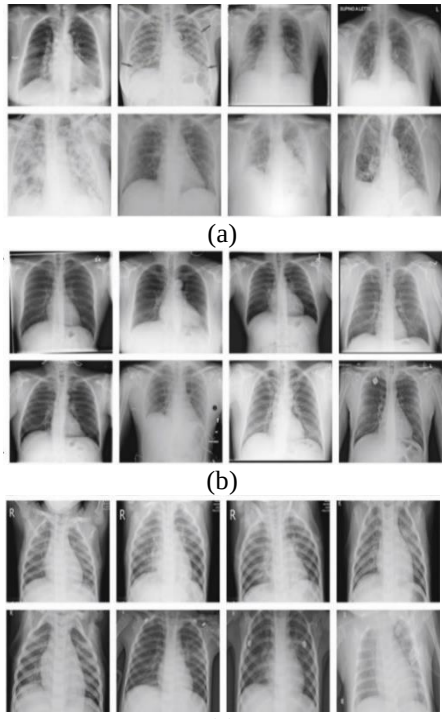

(a) (b) (c)

Figure. 2: (a) COVID, (b) Normal, and (c) VP

4. Results and discussion

In this segment, the XRI classifying outcomes of the BMODL-MICM technique are validated on the XRI dataset in the Kaggle storage [22]. The database comprises 3000 images with three classes, as represented in Table 1. Fig. 2 illustrates the instance images.

Fig. 3 illustrates the classification outputs of the BMODL-MICM technique under the sample dataset.

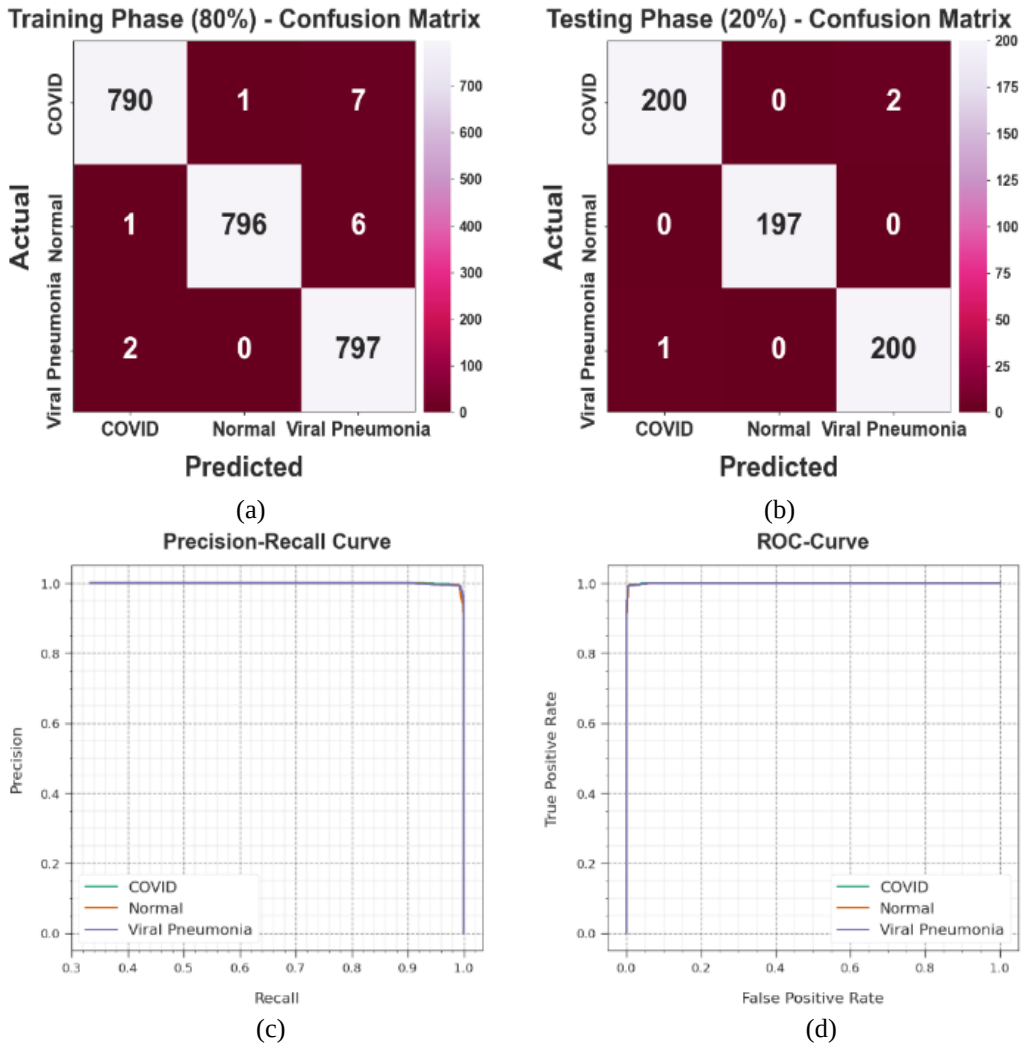

Figure. 3 Classification result of: (a) and (b) Confusion matrix of 80:20, (c) PR curve, and (d) ROC curve

Table 2. XRI classifier output of BMODL-MICM system on 80:20 of TRP/TSP

Class	$Accu_y$	$Prec_n$	$Reca_l$	F_{Score}	MCC
Training (80%)					
COVID	99.54	99.62	99.00	99.31	98.97
Normal	99.67	99.87	99.13	99.50	99.25
VP	99.38	98.40	99.75	99.07	98.60
Average	**99.53**	**99.30**	**99.29**	**99.29**	**98.94**
Testing (20%)					
COVID	99.50	99.50	99.01	99.26	98.88
Normal	100.00	100.00	100.00	100.00	100.00
VP	99.50	99.01	99.50	99.26	98.88
Average	**99.67**	**99.50**	**99.50**	**99.50**	**99.25**

Fig. 3a portrayed the confusion matrices offered by the BMODL-MICM technique on 80 percent of TRP. The figure illustrated that the BMODL-MICM method has identified the instances of 790: COVID, 796: normal, and 797: VP. Besides, Fig. 3b describes the confusion matrices given by the BMODL-MICM method on 20 percent of TSP. The figure represented that the BMODL-MICM method has identified instances of 200: COVID, 197: normal, and 200: VP.

Similarly, Fig. 3c validates the PR evaluation of the BMODL-MICM method. The figures depicted that the BMODL-MICM approach had attained greater PR achievement under the total classes. Lastly, Fig. 3d shows the ROC evaluation of the BMODL-MICM methodology. The figure shows that the BMODL-MICM methodology has greater outcomes with greater values of ROC under three class labelling.

In Table 2 and Figs. 4-5, the comprehensive XRI classifying output of the BMODL-MICM model with 80:20 of TRP/TSP is demonstrated.

The figure inferred that the BMODL-MICM model reaches better performance under three classes. With 80% of TRP, the BMODL-MICM technique

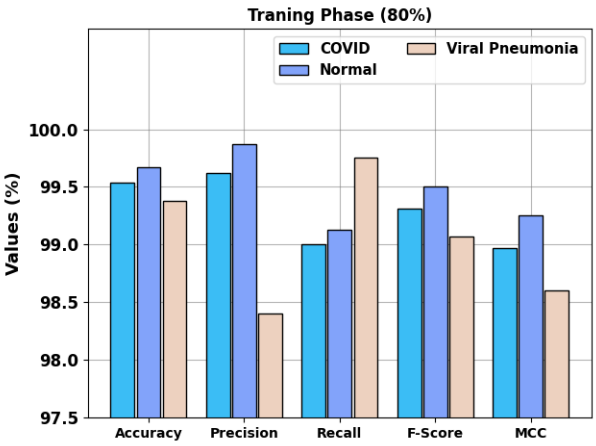

Figure. 4 XRI classifier outcome of BMODL-MICM approach on 80% of TRP

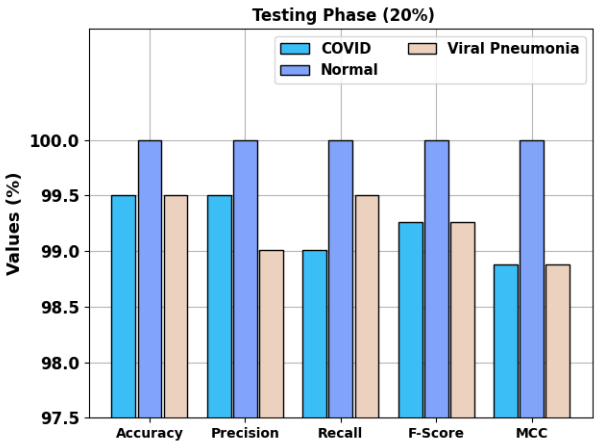

Figure. 5 XRI classifier outcome of BMODL-MICM approach on 20% of TSP

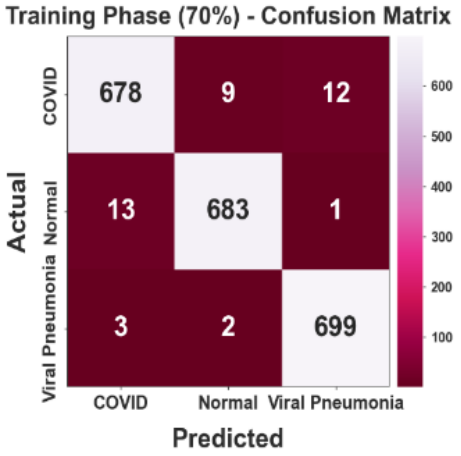

(a)

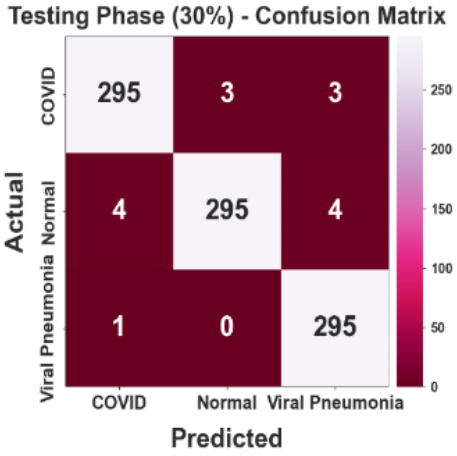

(b)

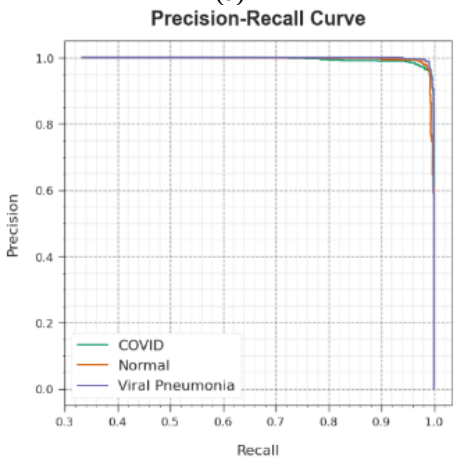

(c)

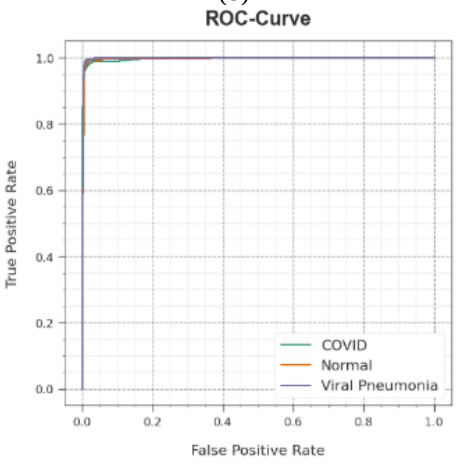

(d)

Figure. 6 Classification result of: (a) and (b) Confusion matrix of 70:30, (c) PR curve, and (d) ROC curve

attains an average $accu_y$ of 99.53%, $prec_n$ of 99.30%, $reca_l$ of 99.29%, F_{score} of 99.29%, and MCC of 98.94%. In the meantime, with 20% of TSP, the BMODL-MICM technique reaches an average $accu_y$ of 99.67%, $prec_n$ of 99.50%, $reca_l$ of 99.50%, F_{score} of 99.50%, and MCC of 99.25%.

Fig. 6 reveals the classification outputs of the BMODL-MICM method under the testing dataset. Fig. 6a describes the confusion matrices presented by the BMODL-MICM algorithm on 70 percent of TRP. The figure depicted that the BMODL-MICM algorithm has recognized instances of 678: COVID, 683: normal, and 699: VP. Also, Fig. 6b represents the confusion matrices presented by the BMODL-

Table 3. XRI classification result of BMODL-MICM technique on 80 and 20 percent of TRP/TSP

Class	$Accu_y$	$Prec_n$	$Reca_l$	F_{Score}	MCC
Training (70%)					
COVID	98.24	97.69	97.00	97.34	96.03
Normal	98.81	98.41	97.99	98.20	97.31
VP	99.14	98.17	99.29	98.73	98.09
Average	**98.73**	**98.09**	**98.09**	**98.09**	**97.14**
Testing (30%)					
COVID	98.78	98.33	98.01	98.17	97.25
Normal	98.78	98.99	97.36	98.17	97.26
VP	99.11	97.68	99.66	98.66	98.01
Average	**98.89**	**98.34**	**98.34**	**98.33**	**97.51**

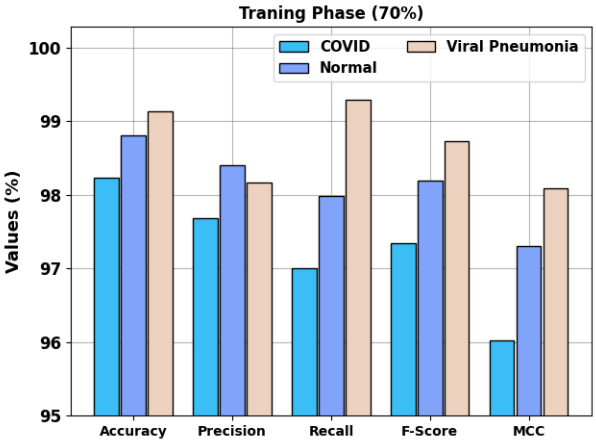

Figure. 7 XRI classifier outcome of BMODL-MICM approach on 70% of TRP

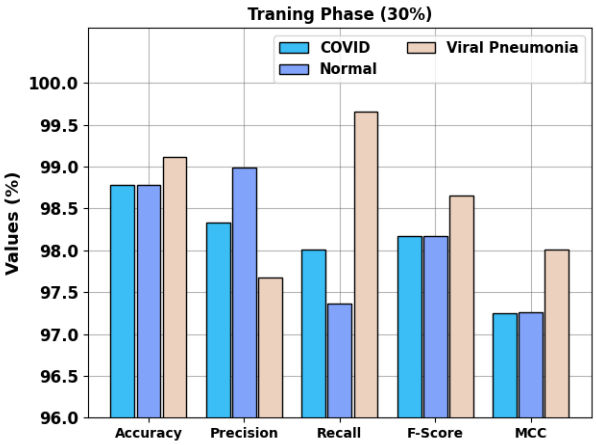

Figure. 8 XRI classifier outcome of BMODL-MICM approach on 30% of TSP

MICM system on 30 percent of TSP. The figure depicted that the BMODL-MICM approach has recognized instances of 295: COVID, 295: normal, and 295: VP. Also, Fig. 6c illustrates the PR evaluation of the BMODL-MICM model. The figures illustrated that the BMODL-MICM model had attained higher PR achievement under the total

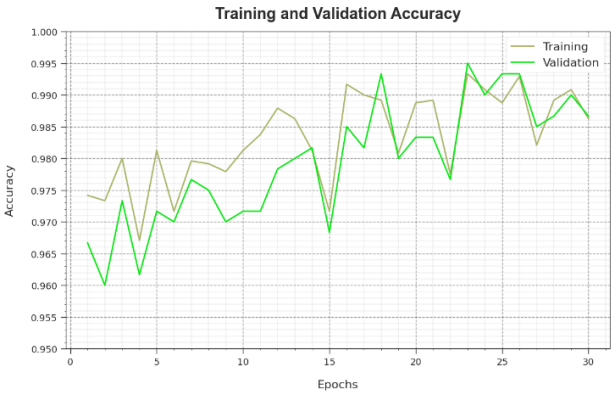

Figure. 9 Accuracy curve of the BMODL-MICM approach

Figure. 10 Loss curve of the BMODL-MICM approach

Table 4. Relative result of BMODL-MICM algorithm with other recent models

Methods	Accuracy	Precision	Recall
SqueezeNet	92.96	91.73	95.10
TLSqueezeNet	96.44	96.08	96.84
VGG19	93.30	91.78	94.73
TLResNet2	98.44	97.97	97.94
ResNet1	97.23	96.74	97.43
BMODL-MICM	99.67	99.50	99.50

classes. At last, Fig. 6d exemplifies the ROC study of the BMODL-MICM technique. The figure portrayed that the BMODL-MICM technique has greater outputs with maximum values of ROC under three class labelling.

In Table 3 and Figs. 7-8, the comprehensive XRI classification outcome of the BMODL-MICM methodology with 70 and 30 percent of TRP/TSP is demonstrated. The figure inferred that the BMODL-MICM methodology attains improved performance under three classes. As a sample, with 70 percent of TRP, the BMODL-MICM approach achieves an

average $accu_y$ of 98.73%, $prec_n$ of 98.09%, $reca_l$ of 98.09%, F_{score} of 98.09%, and MCC of 97.14%. In the meantime, with 30 percent of TSP, the BMODL-MICM approach achieves an average $accu_y$ of 98.89%, $prec_n$ of 98.34%, $reca_l$ of 98.34%, F_{score} of 98.33%, and MCC of 97.51%.

Fig. 9 investigates the accuracy of the BMODL-MICM approach during the process of Training and Validation (T&V) on the trial dataset. The figure notified that the BMODL-MICM approach attains growing values of accuracy over enhancing epochs. Additionally, the growing accuracy of validation over the accuracy of training depicts that the BMODL-MICM method learns effectively on the testing dataset.

The loss study of the BMODL-MICM approach during the time of T&V is depicted on the testing dataset in Fig. 10. The figure indicates that the BMODL-MICM approach attains closer T&V loss values.

In Table 4, a detailed analysis of the BMODL-MICM technique with recent approaches is provided [23, 24].

Fig. 11 demonstrates the results of the BMODL-MICM technique with existing models in terms of $accu_y$. The figure portrayed the higher outcome of the BMODL-MICM methodology with increasing $accu_y$ values. Based on $accu_y$, the BMODL-MICM technique reaches an improving $accu_y$ of 99.67% while the SqueezeNet, TLSqueezeNet, VGG19, TLResNet2, and ResNet1 approaches obtain lesser $accu_y$ values of 92.96%, 96.44%, 93.30%, 98.44%, and 97.23% correspondingly.

Fig. 12 demonstrates the results of the BMODL-MICM technique with existing models in terms of $prec_n$ and $reca_l$. The figure portrayed the higher result of the BMODL-MICM system with increasing

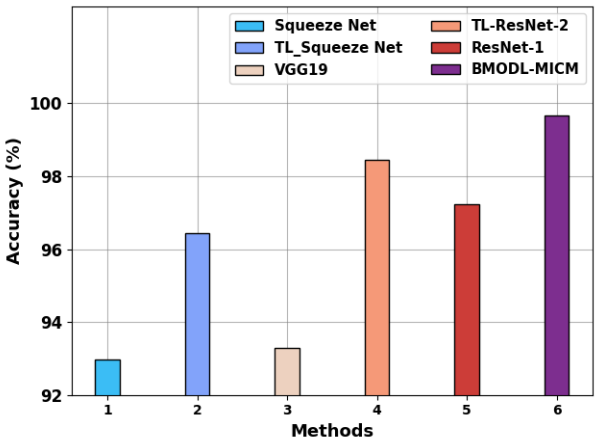

Figure. 11 $Accu_y$ evaluation of BMODL-MICM approach with other current models

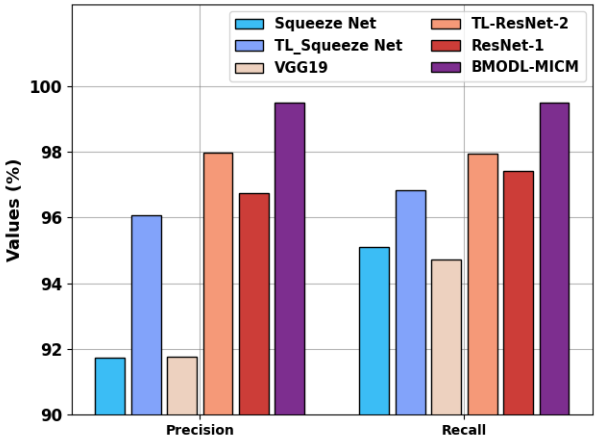

Figure. 12 $Prec_n$ and $reca_l$ evaluation of BMODL-MICM approach with other current models

$prec_n$ and $reca_l$ values. Based on $prec_n$, the BMODL-MICM technique reaches an improving $prec_n$ of 99.50% while the SqueezeNet, TLSqueezeNet, VGG19, TLResNet2, and ResNet1 models obtain minimal $prec_n$ values of 95.10%, 96.84%, 94.73%, 97.94%, and 97.43% correspondingly. At the same time, based on ca_l, the BMODL-MICM technique reaches an improving $reca_l$ of 99.50% while the SqueezeNet, TLSqueezeNet, VGG19, TLResNet2, and ResNet1 systems obtain lesser $reca_l$ values of 91.73%, 96.08%, 91.78%, 97.97% and 96.74% respectively.

5. Conclusion

In this article, an automated XRI classification model named BMODL-MICM technique is presented. This BMODL-MICM model investigates the XRIs carefully and allocates proper class labels to them. To accomplish this, the BMODL-MICM model encompasses WF based noise removal, ShuffleNetv2 feature extractor, BMO based tuning process, and ENN based classification. The application of the BMO model assists the optimal hyperparameter selection of the ShuffleNetv2 technique, which results in maximum performance. The investigational outcomes of the BMODL-MICM approach on the benchmark XRI dataset reported its effectual performance over the other compared methods with respect to various measures. In future, an ensemble voting classifier will be derived to enhance the classification results of the BMODL-MICM system.

Conflict of interest:

The authors declare no conflict of interest.

Author contributions:

Conceptualization, Kumar and Ponnusamy; methodology, Kumar and Ponnusamy; software, Kumar; validation, Kumar; formal analysis, Kumar and Ponnusamy; investigation, Kumar and Ponnusamy; resources, Kumar; data curation, Kumar; writing-original draft preparation, Kumar; writing-review and editing, Kumar and Ponnusamy; visualization, Kumar; supervision, Kumar; project administration, Kumar; funding acquisition, Kumar. All authors have read and gave approval for the final manuscript.

References

[1] M. Constantinou, T. Exarchos, A. G. Vrahatis, and P. Vlamos, "COVID-19 classification on chest X-Ray images using deep learning methods", *International Journal of Environmental Research and Public Health*, Vol. 20, No. 3, p. 2035, 2023.

[2] I. Sirazitdinov, M. Kholiavchenko, T. Mustafaev, Y. Yixuan, R. Kuleev *et al.*, "Deep neural network ensemble for pneumonia localization from a large-scale chest X-Ray database", *Computers & Electrical Engineering*, Vol. 78, pp. 388-399, 2019.

[3] W. Zouch, D. Sagga, A. Echtioui, R. Khemakhem, M. Ghorbel *et al.*, "Detection of COVID-19 from CT and chest X-Ray images using deep learning models", *Annals of Biomedical Engineering*, Vol. 50, No. 7, pp. 825-835, 2022.

[4] D. Keidar, D. Yaron, E. Goldstein, Y. Shachar, A. Blass *et al.*, "COVID-19 classification of X-Ray images using deep neural networks", *European Radiology*, Vol. 31, No. 12, pp. 9654-9663, 2021.

[5] A. Moussaid, N. Zrira, I. Benmiloud, Z. Farahat, Y. Karmoun *et al.*, "On the Implementation of a Post-Pandemic Deep Learning Algorithm Based on a Hybrid CT-Scan/X-Ray Images Classification Applied to Pneumonia Categories", *Healthcare*, Vol. 11, p. 662, 2023.

[6] F.A. Zeidabadi and M. Dehghani, "POA: Puzzle Optimization Algorithm", *International Journal of Intelligent Engineering and Systems*, Vol. 15, No. 1, 2022, doi: 10.22266/ijies2022.0228.25.

[7] P. D. Kusuma and A. L. Prasasti, "Guided Pelican Algorithm", *International Journal of Intelligent Engineering and Systems*, Vol. 15, No. 6, 2022 DOI: 10.22266/ijies2022.1231.18.

[8] P. D. Kusuma and M. Kallista, "Stochastic Komodo Algorithm", *International Journal of Intelligent Engineering and Systems*, Vol. 15, No. 4, 2022, doi: 10.22266/ijies2022.0831.15.

[9] P. D. Kusuma and M. Kallista, "Quad Tournament Optimizer: A Novel Metaheuristic Based on Tournament Among Four Strategies", *International Journal of Intelligent Engineering and Systems*, Vol. 16, No. 2, 2023, doi: 10.22266/ijies2023.0430.22.

[10] P. D. Kusuma and A. Novianty, "Multiple Interaction Optimizer: A Novel Metaheuristic and Its Application to Solve Order Allocation Problem", *International Journal of Intelligent Engineering and Systems*, Vol. 16, No. 2, 2023, doi: 10.22266/ijies2023.0430.35.

[11] A. K. Verma, I. Vamsi, P. Saurabh, R. Sudha, G. R. Sabareesh *et al.*, "Wavelet and deep learning-based detection of SARS-nCoV from thoracic X-Ray images for rapid and efficient testing", *Expert Systems with Applications*, Vol. 185, p. 115650, 2021.

[12] T. K. K. Ho and J. Gwak, "Utilizing knowledge distillation in deep learning for classification of chest X-Ray abnormalities", *IEEE Access*, Vol. 8, pp. 160749-160761, 2020.

[13] L. Tanzi, E. Vezzetti, R. Moreno, A. Aprato, A. Audisio *et al.*, "Hierarchical fracture classification of proximal femur X-Ray images using a multistage Deep Learning approach", *European Journal of Radiology*, Vol. 133, p. 109373, 2020.

[14] S. Bharati, P. Podder and M. R. H. Mondal, "Hybrid deep learning for detecting lung diseases from X-Ray images", *Informatics in Medicine Unlocked*, Vol. 20, p. 100391, 2020.

[15] X. Chen, J. Li, Y. Zhang, Y. Lu and S. Liu, "Automatic feature extraction in X-Ray image based on deep learning approach for determination of bone age", *Future Generation Computer Systems*, Vol. 110, pp. 795-801, 2020.

[16] R. Kundu, R. Das, Z. W. Geem, G. T. Han, and R. Sarkar, "Pneumonia detection in chest X-Ray images using an ensemble of deep learning models", *PloS One*, Vol. 16, No. 9, 2021, doi: 10.1371/journal.pone.0256630.

[17] F. Uysal, F. Hardalaç, O. Peker, T. Tolunay, and N. Tokgöz, "Classification of shoulder X-Ray images with deep learning ensemble models", *Applied Sciences*, Vol. 11, No. 6, p. 2723, 2021.

[18] B. M. Ferzo and F. M. Mustafa, "Image Denoising in Wavelet Domain Based on Thresholding with Applying Wiener Filter", In: *Proc. of 2020 International Conference on Computer Science and Software Engineering (CSASE)*, Duhok, Iraq, pp. 106-111, 2020, doi: 10.1109/CSASE48920.2020.9142091.

[19] Y. Fu, Y. Lu, and R. Ni, "Chinese Lip-Reading

Research Based on ShuffleNet and CBAM", *Applied Sciences*, Vol. 13, No. 2, p. 1106, 2023.
[20] Z. Mustaffa and M. H. Sulaiman, "Stock Price Predictive Analysis: An Application of Hybrid Barnacles Mating Optimizer with Artificial Neural Network", *International Journal of Cognitive Computing in Engineering*, 2023, doi: 10.1016/j.ijcce.2023.03.003
[21] S. Ding, Y. Zhang, J. Chen, and W. Jia, "Research on using genetic algorithms to optimize Elman neural networks", *Neural Computing and Applications*, Vol. 23, pp. 293-297, 2013.
[22] https://www.kaggle.com/tawsifurrahman/covid19-radiography-database
[23] S. H. Khan, A. Sohail, A. Khan, M. Hassan, Y. S. Lee *et al.*, "COVID-19 detection in chest X-Ray images using deep boosted hybrid learning", *Computers in Biology and Medicine*, Vol. 137, p. 104816, 2021.
[24] M. Ragab, S. Alshehri, N. A. Alhakamy, W. Alsaggaf, H. A. Alhadrami *et al.*, "Machine Learning with Quantum Seagull Optimization Model for COVID-19 Chest X-Ray Image Classification", *Journal of Healthcare Engineering*, 2022, doi:10.1155/2022/6074538.